Monthly Notices
of the
ROYAL ASTRONOMICAL SOCIETY

MNRAS **488,** 4816–4830 (2019) doi:10.1093/mnras/stz1976
Advance Access publication 2019 July 22

Evidence for rapid disc formation and reprocessing in the X-ray bright tidal disruption event candidate AT 2018fyk

T. Wevers,[1★] D. R. Pasham,[2] S. van Velzen,[3,4] G. Leloudas,[5] S. Schulze,[6] J. C. A. Miller-Jones,[7] P. G. Jonker,[8,9] M. Gromadzki,[10] E. Kankare,[11] S. T. Hodgkin,[1] Ł. Wyrzykowski,[10] Z. Kostrzewa-Rutkowska,[8] S. Moran,[11,12] M. Berton,[13,14] K. Maguire,[15,16] F. Onori,[17] S. Mattila[11] and M. Nicholl[18,19]

Affiliations are listed at the end of the paper

Accepted 2019 July 15. Received 2019 July 15; in original form 2019 March 22

ABSTRACT

We present optical spectroscopic and *Swift* UVOT/XRT observations of the X-ray and UV/optical bright tidal disruption event (TDE) candidate AT 2018fyk/ASASSN–18ul discovered by ASAS–SN. The *Swift* light curve is atypical for a TDE, entering a plateau after ∼40 d of decline from peak. After 80 d the UV/optical light curve breaks again to decline further, while the X-ray emission becomes brighter and harder. In addition to broad H, He, and potentially O/Fe lines, narrow emission lines emerge in the optical spectra during the plateau phase. We identify both high-ionization (O III) and low-ionization (Fe II) lines, which are visible for ∼45 d. We similarly identify Fe II lines in optical spectra of ASASSN–15oi 330 d after discovery, indicating that a class of Fe-rich TDEs exists. The spectral similarity between AT 2018fyk, narrow-line Seyfert 1 galaxies, and some extreme coronal line emitters suggests that TDEs are capable of creating similar physical conditions in the nuclei of galaxies. The Fe II lines can be associated with the formation of a compact accretion disc, as the emergence of low-ionization emission lines requires optically thick, high-density gas. Taken together with the plateau in X-ray and UV/optical luminosity this indicates that emission from the central source is efficiently reprocessed into UV/optical wavelengths. Such a two-component light curve is very similar to that seen in the TDE candidate ASASSN–15lh, and is a natural consequence of a relativistic orbital pericentre.

Key words: accretion, accretion discs – black hole physics – galaxies: nuclei – ultraviolet: galaxies – X-rays: galaxies.

1 INTRODUCTION

Passing within the tidal radius of the supermassive black hole (SMBH) in the centre of a galaxy can lead to a star's demise (Hills 1975; Rees 1988; Phinney 1989). Such cataclysmic events, called tidal disruption events (TDEs), resemble panchromatic cosmic fireworks, with bright emission at wavelengths ranging from radio (Alexander et al. 2016; van Velzen et al. 2016a), IR (Jiang et al. 2016; van Velzen et al. 2016b; Mattila et al. 2018), optical and UV (Gezari et al. 2008; van Velzen et al. 2011; Arcavi et al. 2014; Holoien et al. 2016b; Wyrzykowski et al. 2017) as well as X-rays (Komossa & Bade 1999; Greiner et al. 2000), and even γ rays (Bloom et al. 2011; Cenko et al. 2012). The duration and brightness of such flares depends on the complex dynamics of material in the presence of strong gravitational fields (Guillochon & Ramirez-Ruiz 2015; Metzger & Stone 2016). Wide-field surveys such as the Roentgen Satellite (ROSAT) and the X-ray MultiMirror telescope (XMM; Jansen et al. 2001) in X-rays and the Galaxy and Evolution Explorer (GALEX), Sloan Digital Sky Survey (SDSS; Stoughton et al. 2002), the (intermediate) Palomar Transient Factory (PTF; Law et al. 2009) and the All Sky Automated Supernova (ASASSN; Kochanek et al. 2017) surveys in the UV/optical have led to the discovery and characterization, first in archival data and later in near real time, of a few dozen TDEs and even more TDE candidates.

Sparse (or non-existent) temporal data coverage of UV/optical selected TDEs at X-ray wavelengths (and vice versa) inhibit the multiwavelength characterization and subsequently the detailed study of the energetics and dynamics at play. This sparse coverage is the result of a variety of factors, such as the difficulty to perform image subtraction in galactic nuclei, the need for fast and systematic spectroscopic follow-up of nuclear transients, and the limited

★ E-mail: tw@ast.cam.ac.uk

availability of multiwavelength monitoring. Coordinated efforts in recent years have led to significant progress in this respect, and most spectroscopically confirmed TDEs are now observed with the *Swift* X-ray observatory, made possible due to its flexible scheduling system.

Nevertheless, disentangling the dominant emission mechanisms remains a challenge. The thermal soft X-ray emission is thought to originate from a compact accretion disc (e.g. Komossa & Bade 1999; Auchettl, Guillochon & Ramirez-Ruiz 2017) while luminous hard X-ray emission finds it origin in a relativistic jet (Bloom et al. 2011; Cenko et al. 2012). For the UV/optical emission, however, a clear picture has not yet emerged. Shocks due to stream–stream collisions (Piran et al. 2015; Shiokawa et al. 2015) or reprocessing of accretion power in either static (Loeb & Ulmer 1997; Guillochon, Manukian & Ramirez-Ruiz 2014; Roth et al. 2016) or outflowing material (e.g. Strubbe & Quataert 2009; Metzger & Stone 2016; Roth & Kasen 2018) have all been proposed to explain the observations. Dai et al. (2018) proposed a model that can explain both the X-ray and UV/optical observations by suggesting a geometry similar to the active galactic nucleus (AGN) unification model (see also Metzger & Stone 2016), where an optically thick structure in the disc orbital plane or an optically thick super-Eddington disc wind obscures the X-ray emission for certain viewing angles. The presence of Bowen fluorescence lines, which require an X-ray powering source, in several TDEs with X-ray non-detections (Leloudas et al. 2019), support this scenario.

In terms of their optical spectra, TDEs typically show broad (10–20 $\times$ 10^3 km s^{-1}) H and/or He lines (Arcavi et al. 2014), although it is unclear what determines whether a TDE is H-rich, He-rich, or shows both features. Furthermore, while some TDEs show only broad He II emission, the sudden appearance or disappearance of other lines such as He I has been observed (Holoien et al. 2016a). One feature in particular is observed in many TDEs: the broad He II line appears to have an asymmetric shoulder in its blue wing. Moreover, it is often observed to be significantly blueshifted (when fit with a Gaussian line profile), whereas other broad Balmer lines, when present, do not show a similar blueshift. While asymmetric Balmer emission line profiles can be modelled using an elliptical accretion disc model (Liu et al. 2017; Cao et al. 2018; Holoien et al. 2019) or alternatively a spherically expanding medium (Roth & Kasen 2018; Hung et al. 2019), it does not appear to adequately explain the He II line morphology. Leloudas et al. (2019) suggest instead that the asymmetry in the line is due to Bowen fluorescence lines, but this cannot explain *all* cases (e.g. ASASSN–15oi).

Leloudas et al. (2016) were the first to claim that two emission mechanisms were observed in a TDE candidate, namely in the double-peaked light curve of ASASSN–15lh. Although the debate as to the nature of this peculiar transient event is still ongoing (Dong et al. 2016; Godoy-Rivera et al. 2017; Margutti et al. 2017), one explanation focused on the TDE interpretation. Leloudas et al. (2016) claim that the double-peaked light curve can be explained in terms of the fallback and viscous time-scales around a very massive ($\geq 10^8$ $M_\odot$) SMBH. In this case the orbital pericentre of the disrupted star is relativistic, making disc formation very efficient. This can lead to two distinct maxima in the light curve. In fact, van Velzen et al. (2019b) recently demonstrated that a two-phase structure appears to be common for all TDEs, but often the second, more shallow phase is observed a few years after peak. Alternatively, Margutti et al. (2017) invoke a model where a sudden change in the ejecta opacity due to an underlying source of ionizing radiation leads to a double-humped light curve. We will show that the light curve of AT 2018fyk shows a similarly double-humped profile to ASASSN–15lh. We propose that the relatively massive black hole ($\sim 2 \times 10^7$ M_{BH}) for AT2018fyk similarly leads to a relativistic pericentre, speeding up the disc formation process and explaining the similarities.

In this work we present our observations of a new tidal disruption event candidate, AT 2018fyk/ASASSN–18ul, discovered by the All Sky Automated Survey for SuperNovae (ASAS–SN; Shappee et al. 2014). We analyse *Swift*'s UltraViolet/Optical Telescope (UVOT) and X-Ray Telescope (XRT) data together with optical low-resolution spectroscopic observations covering the first 120 d of its evolution. While both the light curve and spectra show features peculiar to known TDEs, in particular a secondary maximum in the UVOT bands and the simultaneous emergence of narrow emission lines (in addition to broad H and He lines), we show that these properties can be explained by the reprocessing of (part of the) X-ray emission into UV/optical photons. While the light curve is similar to ASASSN–15lh, this is the first time that unambiguous evidence for reprocessing is found in the optical spectra of TDEs. This shows that the dynamics of the disruption can leave clear imprints on the light curves. Furthermore, the spectral signatures of reprocessing are strongest during the second maximum in the light curve. This suggests that the X-ray source turned on almost contemporaneously with the initial UV/optical peak, in line with a rapid accretion disc formation scenario.

In Section 2, we present X-ray, UV/optical, and radio observations and describe the data reduction process. We present the spectroscopic and light-curve analysis and results in Section 3, while discussing the implications in Section 4. We summarize our main findings in Section 5.

2 OBSERVATIONS AND DATA REDUCTION

The transient AT 2018fyk/ASASSN–18ul was discovered near the centre of the galaxy LCRS B224721.6−450748 (estimated offset of 0.85 arcsec from the nucleus) by the ASAS–SN survey on 2018 September 8 (MJD 58 369.23). The estimated transient brightness was $g = 17.8$ mag, with a non-detection reported ($g \geq 17.4$ mag) on 2018 August 29. A classification spectrum was taken as part of the extended Public ESO Spectroscopic Survey for Transient Objects (ePESSTO; Smartt et al. 2015) on 2018 September 15, revealing a blue featureless continuum superposed with several broad emission lines, suggesting that the transient was likely a TDE (Wevers et al. 2018).

No high spatial resolution archival imaging is available to constrain the position of the transient with respect to the host galaxy centre of light. Fortunately, *Gaia* Science Alerts (GSA; Hodgkin et al. 2013) also detected the transient (aka Gaia18cyc) at the position (α, δ) = (22:50:16.1, –44:51:53.5) on 2018 October 10, with an estimated astrometric accuracy of $\sim$100 mas.[1] The host galaxy is part of the *Gaia* Data Release 2 (GDR2) catalogue (Gaia Collaboration 2016, 2018), and its position is reported as (α, δ) = (22:50:16.093, –44:51:53.499) with formal uncertainties of 1.1 and 1.5 mas in right ascension and declination, respectively (Lindegren et al. 2018). We note that the GDR2 astrometric_excess_noise parameter is 11 mas, which indicates that the formal errors are likely underestimated (as expected for an extended source, Lindegren et al. 2018). The offset between the transient and host galaxy positions is 15 mas.

[1]This is due to the fact that GSA uses the initial data treatment astrometric solution (Fabricius et al. 2016). In the future, the implementation of an improved astrometric solution could improve this to mas precision.

Table 1. Host galaxy photometry, both observed (above the line) and synthesized in the *Swift* UVOT bands (below the line). The synthetic *Swift* photometry is used for host galaxy subtraction of the light curves.

Filter	*AB* mag
GALEX NUV	21.91 ± 0.4
SkyMapper *g*	17.07 ± 0.05
SkyMapper *r*	16.51 ± 0.14
SkyMapper *i*	15.98 ± 0.04
SkyMapper *z*	15.71 ± 0.18
WISE *W*1	16.27 ± 0.03
WISE *W*2	16.87 ± 0.03
Swift *UVW*2	22.3
Swift *UVM*2	21.9
Swift *UVW*1	20.8
Swift *U*	18.7
Swift *B*	17.4
Swift *V*	16.5

Kostrzewa-Rutkowska et al. (2018) have shown that the mean offset in the *Gaia* data of SDSS galaxies is ∼100 mas, consistent with the mean offset of SDSS galaxies and their GDR2 counterparts. Additionally, we can try to estimate a potential systematic offset between *Gaia* transients and their GDR2 counterparts. To quantify such an offset, we cross-match the ∼7000 published *Gaia* alerts with GDR2 within a search radius of 0.25 arcsec. The offset distribution (angular distance on the sky) is well described by a Rayleigh function, as expected if the uncertainties in right ascension and declination follow a normal distribution. The distance distribution has a median of 62 mas and standard deviation of 40 mas. This represents the potential systematic offset between the coordinate systems and is fully consistent with the 100 mas transient positional uncertainties, indicating that both coordinate systems are properly aligned.

In conclusion, we find an offset between the transient and host galaxy position of 15 ± 100 mas, which corresponds to 17 ± 120 pc at the host redshift. This illustrates the power of *Gaia* for identifying nuclear transients (see also Kostrzewa-Rutkowska et al. 2018 for a detailed investigation), as it firmly constrains AT 2018fyk to the nucleus of the galaxy.

2.1 Host galaxy spectral energy distribution

We determine the host galaxy redshift from the spectra, which show strong Ca II H + K absorption lines, and find $z = 0.059$. This corresponds to a luminosity distance of approximately 275.1 Mpc, assuming a ΛCDM cosmology with $H_0 = 67.11$ km s^{-1} Mpc^{-1}, $\Omega_m = 0.32$, and $\Omega_\Lambda = 0.68$ (Planck Collaboration XVI 2014). No narrow emission lines from the host galaxy are evident, indicating that the event occurred in a quiescent galaxy. We observe H α and H β in absorption, indicating no ongoing star formation. The lack of significant H δ absorption suggests that the galaxy does not belong to the E + A galaxy class (Dressler & Gunn 1983) in which TDEs have been known to be overrepresented (Arcavi et al. 2014; French, Arcavi & Zabludoff 2016). We identify strong absorption lines at λ4303 (*G* band), λ5172 (Mg I *b*, which indicates an old stellar population), λ5284 (Fe II), and the Na I D doublet at 5890 + 5895 Å. Finally, the AllWISE colour *W*1–*W*2 = 0.04 (Cutri & et al. 2014) further indicates that the black hole is most likely inactive (e.g. Stern et al. 2012; Wu et al. 2012).

To measure the galaxy mass and star formation rate (SFR), we model the spectral energy distribution (SED; see Table 1) with the software package LEPHARE version 2.2 (Arnouts et al. 1999; Ilbert et al. 2006).[2] This also allows us to synthesize the host galaxy brightness in the *Swift* bands, which we use to subtract the host galaxy contribution from the TDE light curves. We generate 3.9 × 10^6 templates based on the Bruzual & Charlot (2003) stellar population synthesis models with the Chabrier initial mass function (IMF; Chabrier 2003). The star formation history (SFH) is approximated by a declining exponential function of the form $e^{(-t/\tau)}$, where t is the age of the stellar population and τ the e-folding time-scale of the SFH (varied in nine steps between 0.1 and 30 Gyr). These templates are attenuated with the Calzetti attenuation curve (varied in 22 steps from $E(B-V) = 0$ to 1 mag; Calzetti et al. 2000). LEPHARE accounts for the contribution from the diffuse gas (e.g. H II regions) following the relation between SFR and the line fluxes presented in Kennicutt (1998).

From the best-fitting template spectrum, we derive a host galaxy stellar mass of $\log(M_\star/M_\odot) = 10.2^{+0.5}_{-0.2}$, and a SFR and intrinsic $E(B-V)$ consistent with 0. Using an empirical bulge-to-total (B/T) ratio (Stone et al. 2018) of 0.47 (very similar to the ratio of the PSF to Petrosian *g*-band flux of 0.57) for this galaxy mass, we find an SMBH mass of $2^{+3}_{-1.2} \times 10^7$ M$_\odot$ using the M_{BH}–M_{bulge} relation (Häring & Rix 2004). We synthesize photometry in the *Swift* UVOT filters, which can be found in Table 1, to perform the host subtraction.

2.2 *Swift* X-ray and UV/optical observations

Swift's (Gehrels et al. 2004) UVOT (Roming et al. 2005) and the XRT (Burrows et al. 2005) started monitoring AT 2018fyk on MJD 58 383.7, approximately 8 d after the classification spectrum was taken and 14 d after the reported discovery (Brimacombe et al. 2018) by the ASAS–SN survey. Between 2018 September 22 and 2019 January 8, 52 monitoring observations were made with an average observing cadence varying between 2 and 4 d. *Swift* could not observe the source after 2019 January 8 due to Sun pointing constraints. We removed two observations (obsIDs: 00010883004 and 00010883038) from further analysis as they had limited XRT exposure (∼10 s) and lacked UVOT data. Fig. 1 shows an X-ray image of AT 2018fyk's field of view as observed with *Swift*/XRT.

The XRT observations were all performed in photon counting (PC) mode, and were reduced using the latest version of the *Swift* XRTPIPELINE provided as part of HEASOFT 6.25 analysis package. Source counts were extracted using a circular aperture with a radius of 47 arcsec, and corrected for the background contribution using an annulus with an inner and outer radius of 70 and 250 arcsec, respectively. Count rates are converted to an unabsorbed 0.3 – 8 keV flux using a conversion factor of 4.4 × 10^{-11}, derived from the average count rate and flux in the stacked X-ray observations, and assuming a Galactic n_H column of 0.012 × 10^{20} cm^{-2}.

We note that no source is detected in archival ROSAT observations down to a limit of ∼5 × 10^{-4} cts s^{-1} (Boller et al. 2016). Using the webPIMMS tool,[3] this corresponds to a flux limit of 5 × 10^{-15} erg cm^{-2} s^{-1} (0.3–8 keV, assuming a power-law model with $n = 2$ typical for AGN), which translates to an upper limit for the host X-ray luminosity of ∼5 × 10^{40} erg s^{-1} (a blackbody model with kT = 0.1 keV results in an upper limit of 1.5 × 10^{40} erg s^{-1}).

We used the `uvotsource` task to construct UVOT light curves, using a 5 arcsec aperture in all filters to estimate the source brightness. Background levels were estimated by using a circular

[2] http://www.cfht.hawaii.edu/~arnouts/LEPHARE/lephare.html
[3] https://heasarc.gsfc.nasa.gov/cgi-bin/Tools/w3pimms/w3pimms.pl

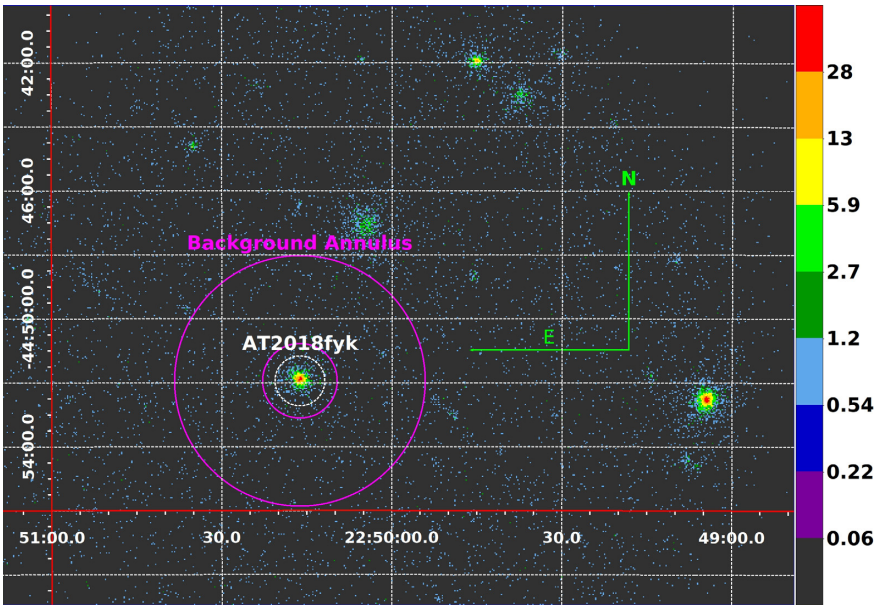

Figure 1. X-ray (0.3–8.0 keV) image of AT 2018fyk's *Swift*/XRT field of view. The source extraction region is indicated by a white dashed circle with a radius of 47 arcsec. The background count rates from each XRT exposure were estimated within an annular region (magenta) with inner and outer radii of 70 and 235 arcsec, respectively. The green arrows are each 300 arcsec.

Table 2. Observational set-ups, observing dates, and exposure times of the optical long-slit EFOSC2 spectra of AT 2018fyk. A 1 arcsec slit was used for all observations. The mean MJD is given for observations taken within the same night.

Grating	Obs date	MJD	Seeing (arcsec)	Exposure time (s)
Gr11	2018-09-16	58377.112	1.1	2 × 1800
Gr11	2018-10-03	58394.213	1.1	2 × 1800
Gr11	2018-10-18	58409.097	1.2	2700
Gr11	2018-11-01	58423.071	1.1	2700
Gr11	2018-11-15	58437.060	0.7	2 × 2400
Gr11	2018-12-03	58455.141	1.1	2 × 2400
Gr13	2018-12-16	58468.090	1.2	2700
Gr13	2018-12-17	58469.059	1.1	2700
Gr13	2019-01-01	58 484.030	0.8	2700
Gr11	2019-01-09	58 492.061	0.9	2700

region with radius of 50 arcsec centred on a nearby empty region of sky (Table A1).

2.3 Optical spectroscopy

Optical spectroscopic observations were obtained with the New Technology Telescope (NTT) located at La Silla, Chile using the ESO Faint Object Spectrograph and Camera (EFOSC2; Buzzoni et al. 1984) instrument with the gr11 and gr13 grisms in combination with a 1 arcsec slit. All observations were obtained as part of the ePESSTO program. We present the observing log including observing dates, set-ups, and exposure times in Table 2.

We reduce the spectroscopic data with IRAF. Standard tasks such as a bias subtraction and flat-field correction are performed first, after which we optimally extract the spectra (Horne 1986) and apply a wavelength calibration using HeAr arc lamp frames. The typical spectral resolution obtained with the gr11 and gr13 set-ups and a 1 arcsec slit for slit-limited observing conditions is $R \sim 250$ and 190 at 4000 Å, respectively (but see Table 2 for the average conditions of each observation; in seeing-limited conditions the resolution increases linearly with the average seeing). Standard star observations are used to perform the flux calibration and correct for atmospheric extinction. Given that the Galactic extinction along the line of sight is negligible, we do not try to correct for this effect. Finally, a telluric correction based on the standard star observations is applied to remove atmospheric absorption features. This is particularly useful to remove the λ 6800 Å absorption features located in the blue wing of the Hα emission line profile. Multiple spectra taken on the same night are averaged, with weights set to the overall SNR ratio between the spectra. The spectra taken on 2018 December 16 and 2018 December 17 are also averaged due to the relatively low SNR of individual exposures. The resulting spectra are shown in Fig. 2, where the flux levels have been scaled to improve the readability of the plot.

2.4 Radio observations

We observed AT 2018fyk with the Australia Telescope Compact Array (ATCA) over three epochs between 2018 September 19 and 2018 November 22, under program code C3148. The observations were taken in the 750C, 6A, and 6B configurations, respectively (see Table 3). While all three are east–west configurations, the former has the inner five antennas at a maximum baseline of 750 m, with the sixth antenna located some 4.3 km away. This isolated antenna was therefore not used when imaging the first epoch, due to the possibility of artefacts arising from the large gap in *uv*-coverage. In all cases we observed in the 15-mm band, using two 2048-MHz frequency chunks (each comprising 2048 1-MHz channels) centred at 16.7 and 21.2 GHz. We used the standard calibrator PKS 1934−638 (Bolton, Gardner & Mackey 1964) as a bandpass calibrator and to set the flux density scale. To solve for the time-dependent complex gains, we used the extragalactic calibrator source QSO B2311−452 (4.23° away; Veron-Cetty & Veron 1983) in the first epoch, and QSO B2227−445 (3.29°

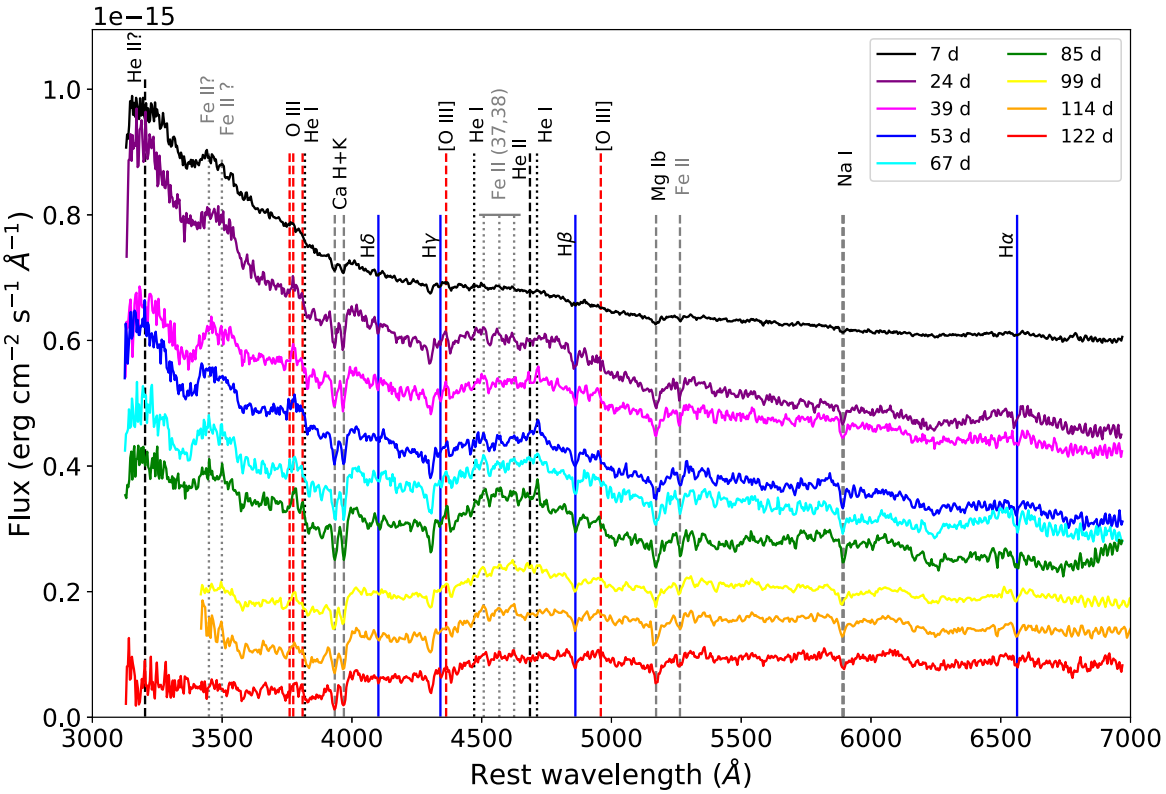

Figure 2. Spectral sequence of AT 2018fyk taken with the NTT. Emission lines are marked by vertical lines: H Balmer series (solid blue), He II (dashed black), He I (dotted black), [O III] (solid red), and Fe II (dotted grey). Host galaxy lines such as Ca H + K, Mg I b and Na D absorption lines are marked by dashed grey lines. The epochs are given with respect to the discovery epoch.

Table 3. ATCA radio observations of AT 2018fyk. We report the time range that the array was on source, and the MJDs of the mid-times of the observations. Flux density upper limits are obtained by stacking both frequency bands together, and are given at the 3σ level.

Date	Time (UT)	MJD	Config.	Flux density (μJy)
2018-09-19	12:36–19:53	58380.68	750C	<38
2018-10-16	10:04–13:28	58407.49	6A	<74
2018-11-22	05:24–08:28	58444.29	6B	<53

away; Savage, Bolton & Wright 1977) for the two subsequent epochs, as appropriate for the relevant array configurations. We used the Common Astronomy Software Application (CASA v.5.1.2; McMullin et al. 2007) package for both calibration and imaging of the data, applying standard procedures for ATCA data reduction. AT 2018fyk was not detected in any of the three epochs, with upper limits as given in Table 3.

3 ANALYSIS

We present the X-ray and (host subtracted) UV/optical light curve obtained with *Swift* in Fig. 3. After an initial decline, the UV/optical appears to turn over around 40 d after discovery to a near constant luminosity. This plateau lasts for nearly 50 d, before the UV/optical light curve breaks again to start declining, while the X-rays increase in brightness.

While the flare is still more than 2.5 mag brighter than the host in the UV bands during the last *Swift* epoch, emission in the *B* and *V* bands was significantly contaminated by the host galaxy light even at the earliest epochs.

3.1 SED analysis

We constrain the luminosity, temperature, and radius evolution of AT 2018fyk by fitting a blackbody to the *Swift* UVOT SED at each epoch. Due to significant contamination from the host galaxy in the reddest bands (*B* and *V*), we do not include these data points. Including these bands does not alter the general results of our analysis, but leads to bad fits and unrealistic temperatures at some epochs. We therefore fit a blackbody model to the host subtracted SED consisting of the UV bands and the *U* band, using a maximum likelihood approach and assuming a flat prior for the temperature between 1–5 $\times$ 10^4 K. 1σ uncertainties are obtained through Markov Chain Monte Carlo simulations (Foreman-Mackey et al. 2013). Using the best-fitting temperature at each epoch, we integrate under the blackbody curve from EUV to IR wavelengths to estimate the bolometric UV/optical luminosity. In addition, we also derive the characteristic emission radius at each epoch. We present the integrated UV/optical luminosity, temperature, and radius evolution in Fig. 4, both the epoch measurements and a 15 d binned evolution for clarity. We find a peak luminosity of $3.0 \pm 0.5 \times 10^{44}$ erg s^{-1}, which declines by a factor of 4 over the first 120 d of the flare evolution. The temperature appears roughly constant initially, but there is evidence for an increase at later epochs similar to ASASSN–15oi (Holoien et al. 2016a) and AT2018zr (Holoien et al. 2019; van Velzen et al. 2019a). The radius, on the other hand, stays constant for the first ~70 d at $4.2 \pm 0.4 \times 10^{14}$ cm, after which it decreases

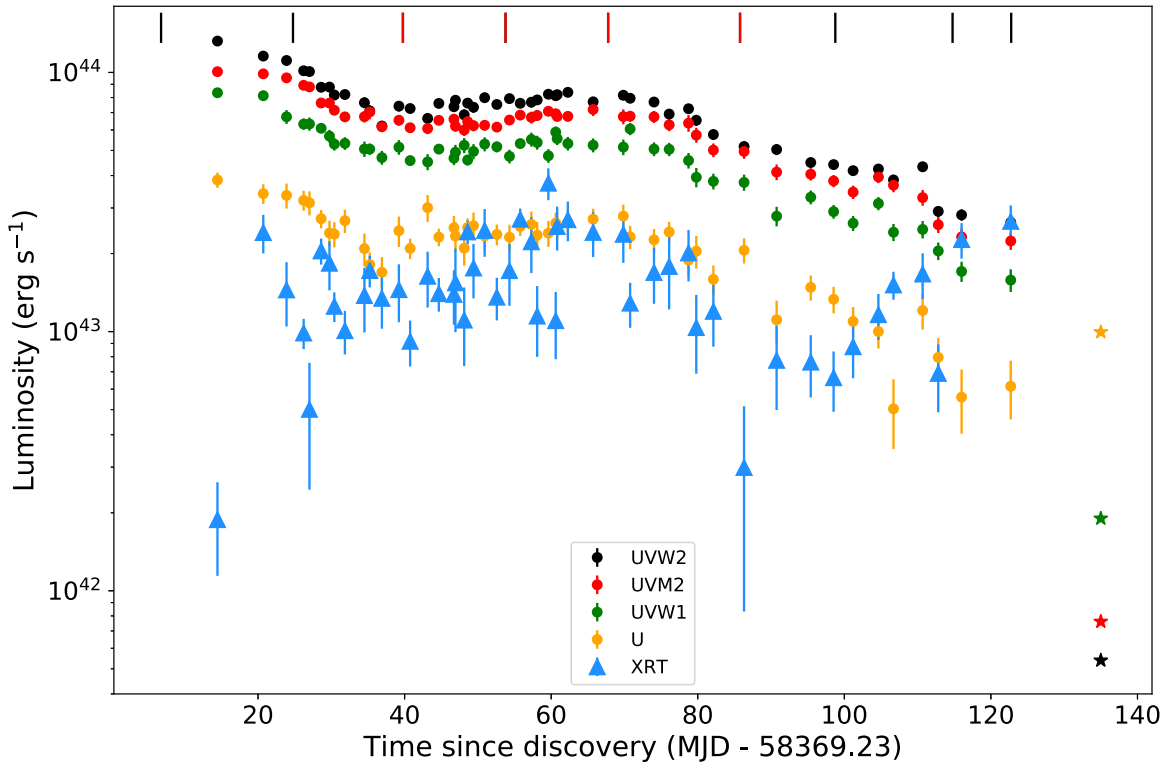

Figure 3. X-ray and host-subtracted UV/optical light curve of AT 2018fyk as observed with *Swift*. The *B* and *V* bands are strongly contaminated by the host galaxy and are omitted for clarity. Unlike other TDE light curves, the UV/optical bands show a plateau phase lasting ∼50 d instead of a steady, monotonic decline. The dashed lines indicate epochs of spectral observations; red dashed lines indicate the epochs showing narrow emission features. Stars indicate the estimated host galaxy brightness.

by a factor of 2 in the span of 50 d. Integrating over the period with *Swift* coverage, we find a total UV/optical energy release of $E_{rad} \sim 1.4 \times 10^{51}$ erg, with the uncertainties dominated by the host subtraction (the observed energy radiated at X-ray wavelengths is $\sim 10^{50}$ erg). These values are all typical when compared to the UV/optical sample of known TDEs (e.g. Hung et al. 2017; Wevers et al. 2017, 2019; Holoien et al. 2019).

3.2 X-ray evolution

AT 2018fyk belongs to a growing sample of UV/optical detected TDE candidates observed to be X-ray bright at early times, together with ASASSN–14li (Holoien et al. 2016b), ASASSN–15oi (Holoien et al. 2016a), and PS18kh/AT2018zr (Holoien et al. 2019; van Velzen et al. 2019a). In addition the source XMMSL1 J0740 (Saxton et al. 2017) was also UV/optical and X-ray bright, although it was detected in X-rays first.

The *Swift* XRT light curve shows variability of a factor 2–5 on a time-scale of days, whereas the UV/optical light curve appears more smooth. During the first epoch the source shows a L_{opt}/L_x ratio ∼150, similar to that of ASASSN–15oi (Gezari, Cenko & Arcavi 2017) and AT2018zr (Holoien et al. 2019; van Velzen et al. 2019a). The X-ray emission then brightens by a factor of ∼10 in 6 d, and remains roughly constant for 25 d. The X-ray emission then displays a plateau similar to the UV/optical evolution, leading to a near constant L_{opt}/L_x ratio for ∼70 d. Between 80 and 100 d after discovery the light curves decline in tandem, after which the X-rays brighten once more while the UV/optical emission keeps declining.

We first rebin the stacked spectrum (total exposure time of 50.2 ks, Fig. 5) to obtain at least 25 counts per spectral bin, appropriate for the use of χ^2 statistics in XSPEC. Fitting this spectrum with a blackbody model (tbabs×zashift×bbodyrad in XSPEC), we find a best-fitting temperature ($\chi^2 = 3.62$ for 43 degrees of freedom) of kT = 121 ± 2 eV, negligible $n_{H,}$ and a normalization factor norm = 675 ± 63. This normalization corresponds to a X-ray photospheric radius of $R_X = 6.5 \pm 0.3 \times 10^{10}$ cm. This in turn corresponds to the innermost stable circular orbit of an accretion disc around a non-spinning SMBH of $\sim 10^5$ $M_\odot$. This is a factor of ∼100 lower than inferred from the bulge mass, and suggests that some obscuration (either from tidal debris or in the host galaxy) occurs. Given the high reduced χ^2 of the fit, we also try an absorbed multitemperature blackbody model (tbabs × zashift × DISKBB) and find $T_{in} = 162 \pm 4$ eV ($\chi^2 = 2.77$ for 43 degrees of freedom). From Fig. 5 (the orange line and markers) it is clear that an additional emission component at energies >1.5 keV is required. Using an absorbed power law + blackbody model (phabs × zashift × (power law + bbodyrad)) increases the goodness of fit significantly ($\chi^2 = 1.39$ for 41 degrees of freedom); this model is shown in blue in Fig. 5. The power-law component contributes ∼ 30 per cent to the unabsorbed X-ray flux. Further analysis is required to investigate the detailed spectral evolution and the potential presence of a harder emission component similar to XMMSL1 J0740 (Saxton et al. 2017), but we defer a more detailed temporal and spectral analysis of the X-ray data to a companion paper.

3.3 Optical spectroscopy

The earliest epochs of spectroscopic observations are dominated by a hot, featureless continuum with several broad emission lines superposed. We identify broad H α, He II λ4686, and potentially He II

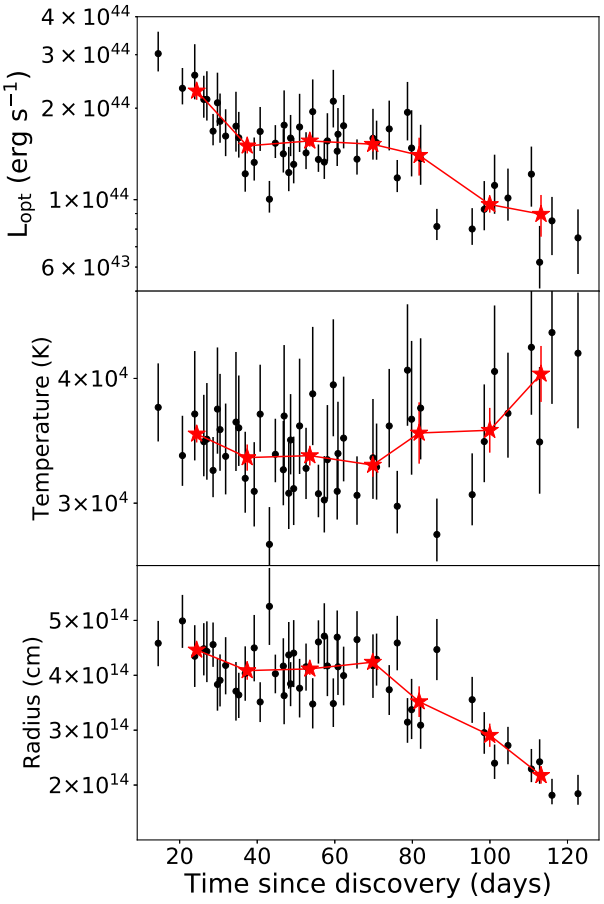

Figure 4. Luminosity, temperature, and blackbody radius evolution of the UV/optical component (black circles) of AT 2018fyk as derived from SED blackbody fitting and *Swift* XRT spectral fitting, respectively. We also show the 15 d binned light curves in red stars.

3203 Å emission lines in the spectrum. In addition, we identify a broad emission line (or lines) in the region 3400–3600 Å. This latter feature can be tentatively identified as O III λ3444 or potentially broad Fe II (λλ3449,3499) lines, although these identifications are uncertain.

AT 2018fyk became unobservable due to Sun constraints before the broad emission lines completely disappeared, hence we cannot perform the host galaxy subtraction in the traditional way. Instead, to identify the nature of the lines and measure their line widths and velocity offsets, we first fit cubic splines to the continuum in MOLLY,[4] masking all prominent emission features, host, and remaining telluric absorption lines. We then subtract the continuum level to reveal the TDE emission line spectrum. Although some host contamination remains, in particular narrow absorption lines (such as the H β absorption trough in the red wing of He II), to first order this removes the featureless blackbody and host galaxy continuum contributions.

Arguably the most interesting features in the optical spectra of AT 2018fyk are the narrow emission lines that appear after the light curve shows a plateau in luminosity. We show the spectrum with the most prominent narrow emission features in Fig. 6, including the most likely line identifications. We identify several

[4]MOLLY is an open source spectral analysis software tool.

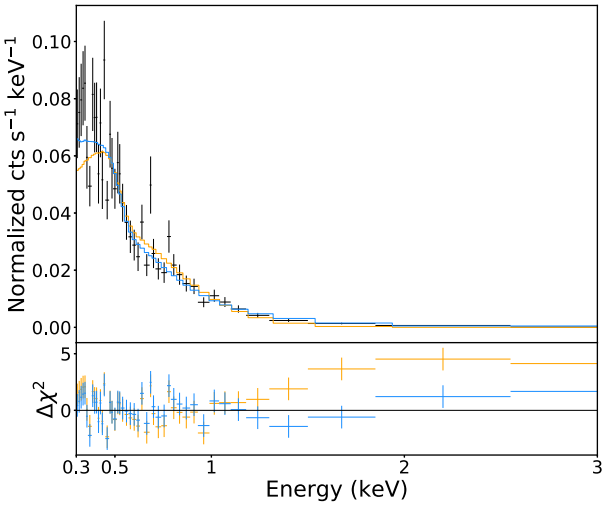

Figure 5. Stacked, rebinned 50.2 ks X-ray spectrum obtained with *Swift*. We overplot the best-fitting absorbed multitemperature blackbody model (DISKBB in XSPEC, orange) with $T_{in} = 162 \pm 4$ eV and negligible n_H. The residuals show that the flux is systematically underestimated at energies >1.5 keV, and an absorbed power law + blackbody model (blue) describes this higher energy emission better.

high-ionization O III lines, and in addition we identify several low-ionization Fe II emission lines (ionization potential ∼8 eV), particularly of the multiplets 37 and 38 with prominent features at λλ4512,4568,4625. We also identify low excitation He I narrow emission lines. Moreover, the increased pseudo-continuum level in Fig. 7 (the green spectrum) may suggest that the emergence of these narrow Fe II lines is accompanied by a broad component as seen in AGN, although this could also be the forest of narrow Fe II lines that is present in the wavelength range 4300–4700 Å. This shows that the spectral diversity of TDEs is even larger than previously identified, with a class of Fe-rich events in addition to the H-, He-, and N-rich TDEs (Arcavi et al. 2014; Blagorodnova et al. 2017; Hung et al. 2017; Leloudas et al. 2019).

The fact that the narrow emission lines are observed only when the light curve shows a plateau phase strongly suggests that they are powered by the same emission mechanism. We also note that we only see narrow emission lines in the blue part of the spectrum. Several transitions of both He I and O III exist at longer wavelengths, and these transitions typically have stronger line strengths (for example in AGN) than the lines we observe in AT 2018fyk.

4 DISCUSSION

4.1 TDE classification

We classified AT 2018fyk as a TDE candidate based on several pieces of evidence.

First, the location is consistent to within ∼100 pc with the nucleus of a galaxy. No signs of activity or star formation are evident from the galaxy colours and no narrow galaxy emission lines are present in the spectra, arguing against a supernova interpretation. Archival X-ray upper limits show that the X-ray emission brightened by a factor of $\gtrsim$1000, making an AGN flare an unlikely interpretation.

Second, the temperature, colour, and blackbody radius evolution of the UV/optical emission are typical of TDEs and unlike any other

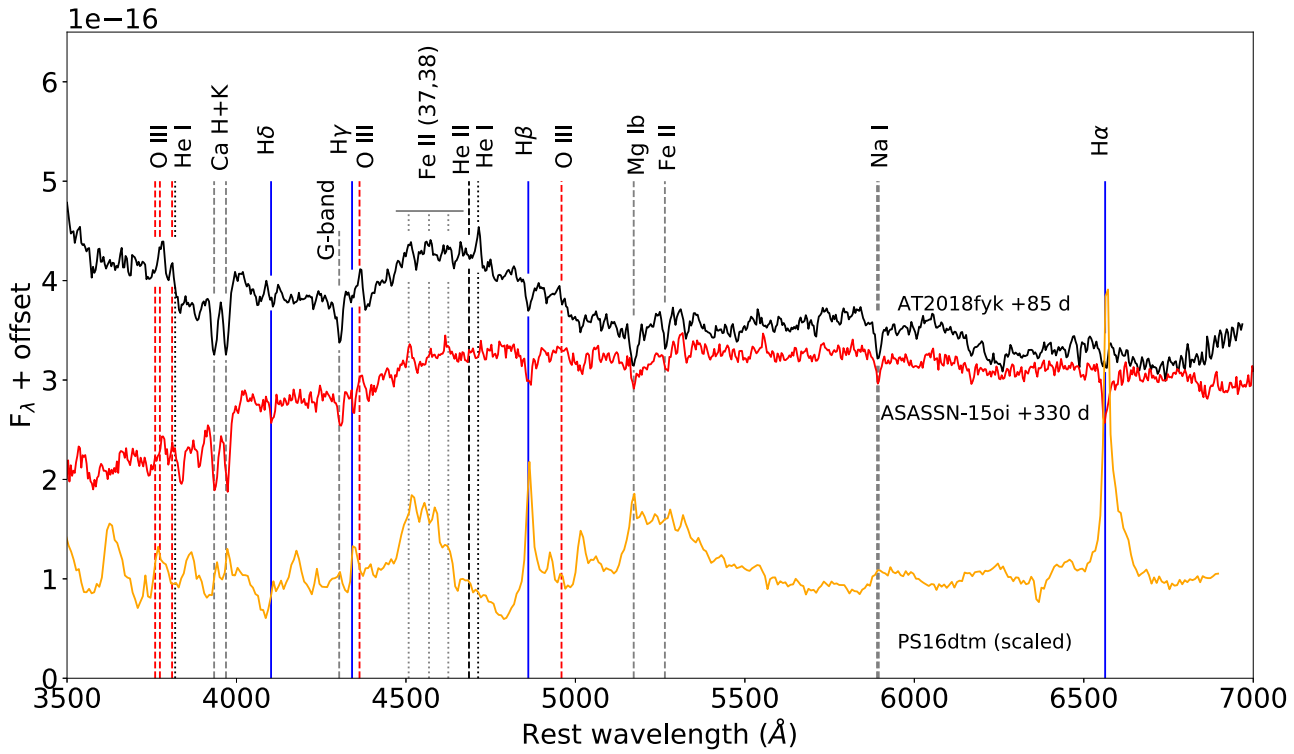

Figure 6. Comparison of the emission line profiles in the He II 4686 region with other events. The narrow Fe II lines are indicated by vertical dotted lines. We show the ASASSN–15oi spectrum in which we identify similarly narrow Fe II lines in red. We also show the spectrum of PS16dtm, which showed very strong Fe II emission.

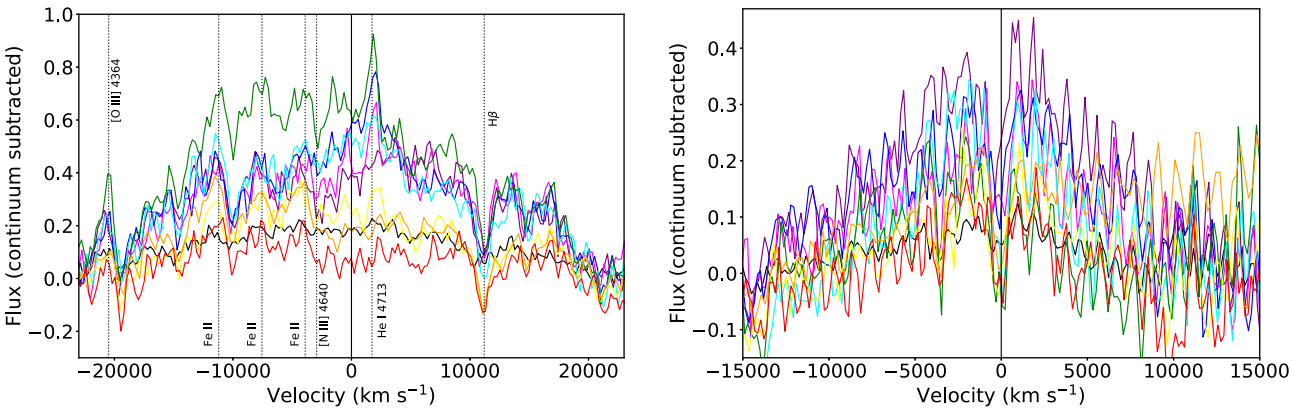

Figure 7. The markedly distinct line profile evolution of the He II 4686 complex and H α (left-hand and right-hand panels, respectively). Relevant emission and absorption lines are marked by vertical lines.

known SN types (Hung et al. 2017; Holoien et al. 2019). The optical spectral evolution is also unlike any SN spectra.

Third, the X-ray emission is an order of magnitude brighter than the brightest X-ray supernovae observed (e.g. Dwarkadas & Gruszko 2012), including superluminous supernovae (Margutti et al. 2018). Moreover, the X-ray spectra of supernovae are not expected to be well described by soft thermal blackbody emission.

The observed properties are broadly consistent with observed TDEs: hot ($T \sim 3.5 \times 10^4$ K) UV/optical blackbody emission that does not cool over 100 d, a near-constant UV/optical colour evolution, a thermal blackbody X-ray component with a temperature of ∼100 eV, broad (∼15 000 km s^{-1}) H and He optical emission lines can all be naturally explained in the TDE scenario (Arcavi et al. 2014; Blagorodnova et al. 2017; Hung et al. 2017; Wevers et al. 2017; Holoien et al. 2019). In the remainder of this Section, we discuss several peculiar features (compared to observations of other TDEs) and how they can be explained in the TDE interpretation.

4.2 Light-curve comparison and secondary maxima

To put the light-curve shape into context, in Fig. 8 we compare the UVW2 light curve of AT 2018fyk with other TDE candidates. The *V*-band (observed) peak absolute magnitude is $V = -20.7$. While the decline is monotonic for the first ∼40 d, similar to the TDEs ASASSN–14li and ASASSN–15oi, the light curve plateaus before declining at a rate similar to ASASSN–14li. This is reminiscent

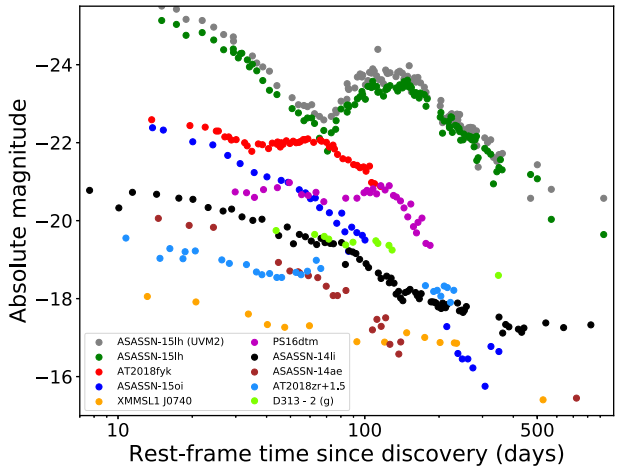

Figure 8. Comparison of the AT 2018fyk UVW2 light curve with other TDEs and TDE candidates near the UV/optical peak. A secondary maximum similar to ASASSN–15lh is observed. In addition, several other sources including AT 2018zr, XMMSL1 J0740, as well as ASASSN–14li show a clear secondary maximum in their light curve.

of the behaviour seen in the TDE candidate ASASSN–15lh, which shows a similar (albeit much more pronounced and much longer) secondary maximum in its light curve. Given the much higher redshift of the latter source, we also show its UVM2 light curve, which probes similar rest wavelengths to the UVW2 filter for the other events. The light curve of PS16dtm, which has been claimed to be a TDE in a NLS1 galaxy (Blanchard et al. 2017), shows a plateau phase but not the characteristic decline from peak leading up to it, as seen in AT 2018fyk and ASASSN–15lh. The UVW2 light curve of XMMSL1 J0740 also shows a similar, though less pronounced, rebrightening phase at ∼150 d (Saxton et al. 2017). For the TDE candidate ASASSN–15lh (but see e.g. Bersten et al. 2016; Dong et al. 2016 for an extreme supernova interpretation), Leloudas et al. (2016) propose that the rebrightening can be explained by taking into account the SMBH mass, which is by far the most massive of the TDE sample ($>10^8$ $M_\odot$). As a consequence, all orbital pericentres become relativistic, even for shallow (low $\beta = R_T/R_p$) stellar encounters. Similar to ASASSN–15lh, we propose that a relativistic pericentre, which leads to two peaks in the light curve (Ulmer 1999), can explain the observations; the first maximum due to shock energy released during stream self-intersections, and the second after disc formation, powered by accretion on to the SMBH.[5] The relatively short time-scale between the first and second maxima in the light curve favours a star from the lower end of the stellar mass distribution, which decreases the semimajor axis and orbital time of the most bound stellar debris (e.g. Dai, McKinney & Miller 2015).

We do not have an accurate black hole mass measurement for the host of AT 2018fyk, but a rough estimate based on the stellar population synthesis suggests that $M_{BH} \sim 2 \times 10^7$ $M_\odot$. Using a simple theoretical prediction of the peak fallback rate (Stone, Sari & Loeb 2013), this will lead to sub-Eddington fallback rates (and hence luminosities, as observed), similar to other TDEs with high black hole masses (e.g. TDE1 and D3-13, Wevers et al. 2017). Given this relatively high black hole mass, for a sub-Eddington peak fallback rate and in the presence of strong shocks during stream self-intersection due to the relativistic pericentre, it is expected that disc formation is more efficient than for non-relativistic pericentres. This holds true for all TDEs around black holes $\gtrsim 10^7$ $M_\odot$, so we inspect the light curves of TDE1 and D3-13 for similar signatures. While the light curve for TDE1 is very sparsely sampled, relatively good coverage is available for D3-13. We find evidence for a rebrightening in the *g*-band light curve ∼100 d after observed peak, as well as a marked flattening in the *r*- and *i*-band light curves. The effects are likely to be strongest at UV wavelengths, which are not covered for D3-13. Nevertheless this suggests that a double-peaked light curve could be a quasi-universal signature of TDEs around massive ($>10^7$ $M_\odot$) black holes, and observations of future TDEs with such black hole masses can confirm this. This interpretation is also consistent with the observed SMBH mass dependence of the late-time UV excess (van Velzen et al. 2019b), where TDEs around higher mass SMBHs have no late-time excess because the early-time emission already includes a large disc contribution due to more efficient circularization.

Our M_{BH} estimate was obtained using scaling relations different from the M–σ relation, and the estimate could potentially be revised downward by up to an order of magnitude (similar to other TDE hosts with M_{BH} estimates from both the M–L and M–σ relations). In that case, the peak fallback rate and luminosity might be super-Eddington and Eddington limited, respectively, and the scenario outlined above becomes unlikely (unless the encounter had a high impact parameter to make the pericentre relativistic). Instead, a variable super-Eddington disc wind (which quenches as the fallback rate decreases) could explain the reprocessing of X-rays into UV/optical emission. When the accretion rate drops further, the disc transitions into a thin disc state, increasing the viscous time-scale and flattening the light curve. We note that a super-Eddington luminosity is not necessarily required for this scenario, as disc transitions can occur even at a few $\times 0.1$ L_{Edd} (e.g. Abramowicz et al. 1988), which is plausible for AT 2018fyk. A velocity dispersion measurement for the host SMBH is required to more accurately measure the black hole mass and differentiate between these scenarios.

Below, we will argue that the second peak in the light curve is powered by efficient reprocessing of energetic photons from the central source into UV/optical emission. As a final note, identifying a TDE candidate with more typical TDE host galaxy parameters (Wevers et al. 2019) but observational characteristics similar to ASASSN–15lh argues in favour of the TDE interpretation of that event (as opposed to a unique SN interpretation). In this interpretation the UV/optical emission and the emergence of X-ray emission after an initial non-detection are explained by the rapid formation of an accretion disc. These similarities and the link between the UV/optical and X-ray emission strengthen the classification of ASASSN–15lh as a TDE (Leloudas et al. 2016; Margutti et al. 2017).

4.3 Detection of low-ionization, narrow emission lines

The broad emission feature near 4686 Å, if only associated with He II 4686 emission, is non-Gaussian in several of the spectra. Comparing its FWHM ∼ 28 000 km s^{-1} with that of the other lines, which range between 10–15 × 10^3 km s^{-1}, it is hard to explain why this line is almost twice as broad if it originates in roughly

[5]Recent work (Bonnerot & Lu 2019), which appeared while this manuscript was under review, suggests that the radiative efficiency of the stream–stream shock could be too low to explain the peak luminosity of observed TDEs (including AT 2018fyk). In the context of their model, the first peak of the light curve could be powered by a 'secondary shock' at the trapping radius, while the plateau is caused by subsequent accretion.

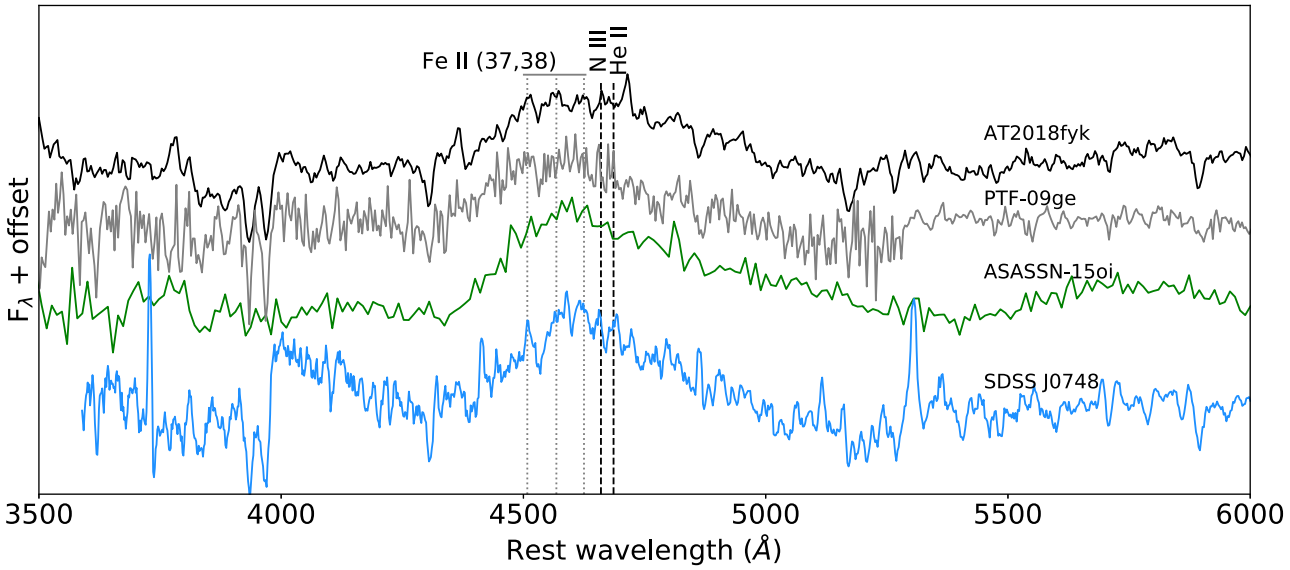

Figure 9. Spectral comparison of AT 2018fyk with ASASSN–15oi, PTF–09ge, and SDSS J0748. All events display a distinct asymmetric line profile in the region around He II λ 4686, which we propose can be explained by multiple Fe II emission lines.

the same physical region. Moreover, the line develops a distinct asymmetric blue shoulder during its evolution (Figs 7 and 9). This suggests, as has been noticed in other TDEs (e.g. Arcavi et al. 2014; Holoien et al. 2016a; Leloudas et al. 2019) that instead this line might be a superposition of several emission features. Holoien et al. (2016a) suggested that part of this line might be explained by He I 4472 in ASASSN–15oi; for AT 2018fyk the line would be redshifted by ∼2500 km s^{-1}, which is not observed for H α and He II. Leloudas et al. (2019) explain the asymmetry in some TDEs as a consequence of Bowen fluorescence lines, but we do not observe the characteristic N III λλ4097,4103 feature that is expected in this case. This suggests that in AT 2018fyk and potentially other TDEs such as ASASSN–15oi (see fig. 4 in Leloudas et al. 2019), Bowen fluorescence lines do not provide a satisfactory explanation. Another alternative, suggested by Roth & Kasen (2018), is outflowing gas that is optically thick to electron scattering, which can produce blueshifted emission peaks and asymmetric red wings in the line profiles.

The emergence of the narrow spectral lines in AT 2018fyk (Fig. 6) allows us to identify the emission in this blue shoulder as Fe II multiplet 37,38 emission lines. These are the strongest optical Fe II multiplet lines, although depending on the excitation mechanism one might also expect emission in the NIR around 1 μm (Marinello et al. 2016), which is unfortunately not covered by our spectra. Given the similarity of the line profiles, we propose that the origin of the blue bump near He II 4686 in the other two events shown in Fig. 9, ASASSN–15oi and PTF–09ge, is likewise Fe II emission, making these events part of an *Fe-rich* class of TDEs. We have also included the coronal line emitter and TDE candidate SDSS J0748 (Yang et al. 2013) for comparison because the line shape is remarkably similar.

These low ionization lines have been detected in AGNs (e.g. Lawrence et al. 1988; Graham, Clowes & Campusano 1996), with EWs that can exceed those of He II 4686. Although the excitation mechanism(s) in AGN is somewhat ambiguous, photoionization (Kwan & Krolik 1981), Ly α resonance pumping (Sigut & Pradhan 1998), and collisional excitation (depending on the particle density) have all been proposed to contribute to some extent to produce these transitions (Baldwin et al. 2004). Their strength is closely associated with the Eddington fraction in AGN (Boroson & Green 1992; Kovačević, Popović & Dimitrijević 2010). While the narrow Fe II lines are thought to originate from a well-defined region in between the broad-line region (BLR) and narrow-line region (NLR), the emission region of the broad component is not currently well constrained (Dong et al. 2011). One possibility is that it originates from the surface of the AGN accretion disc (Zhang, Dultzin-Hacyan & Wang 2006); further evidence for an origin in the accretion disc comes from cataclysmic variables (e.g. Roelofs et al. 2006). Interestingly, Dong et al. (2010) showed that while optical Fe II emission is prevalent in type 1 AGN, it is not observed in type 2 AGN. This suggests that the emission region is located within the obscuring torus.

More generally, the emission region is likely a partially ionized region, where the ionizing photons come from a central X-ray source (Netzer & Wills 1983). Incidentally, some of the strongest optical Fe II lines are observed in narrow-line Seyfert 1 (NLS1) galaxies (e.g. Osterbrock & Pogge 1985), which are typically characterized by a significant soft X-ray excess below 1.5–2 keV, rapid X-ray flux, and spectral variability (see e.g. the review by Gallo 2018) and potentially accreting at high fractions of their Eddington rate (Rakshit et al. 2017). Another interesting resemblance is their preferred black hole mass range, which is $<10^8$ M_{BH} for both TDEs and NLS1s (Peterson 2011; Berton et al. 2015; Chen et al. 2018). These properties are all remarkably similar to those expected/observed for TDEs.

In particular, the TDE candidate PS16dtm was suggested to be a TDE in an active galaxy (Blanchard et al. 2017); the spectrum resembles that of NLS1 galaxies, showing several optical Fe II lines (Fig. 6). PS1-10adi, another TDE candidate in an AGN, was also observed to produce transient Fe II optical emission at late times (Kankare et al. 2017); similar features were also observed in the TDE candidates and extreme coronal line emitters SDSS J0748 and SDSS J0952 (Wang et al. 2011; Yang et al. 2013). These events all occurred around active black holes, so establishing their TDE nature is more ambiguous. The resemblance of AT 2018fyk to some of these events shows that stellar disruptions can create (temporary)

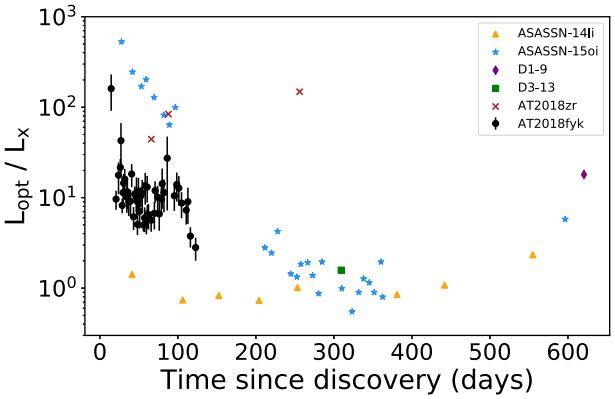

Figure 10. UV/optical to X-ray luminosity ratio for AT 2018fyk, as well as several other X-ray bright TDEs. Data taken from Gezari et al. (2017) and van Velzen et al. (2019a).

circumstances very similar to those in NLS1 AGN even around dormant SMBHs, and that instead of several distinct classes there may be a continuum of nuclear transient events intermediate to 'clean' TDEs and 'clean' AGN flares.

Unlike the high-ionization narrow lines such as O III (which are thought to form within the ionization cone of the central X-ray source in AGN), Fe II emission requires an obscuring medium with significant particle density and optical depth as well as heating input into the gas. The presence of these Fe II lines in the spectra of AT 2018fyk indicates that at least part of the gas is optically thick, while the X-ray spectrum shows that a bright, soft X-ray source is present, making the conditions in this TDE similar to that in NLS1 nuclei.

We inspect publicly available spectra of other TDEs, and find that the presence of narrow Fe II lines is not unique to AT 2018fyk. We identify similar emission lines consistent with the same Fe II multiplet 37,38 lines in optical spectra of ASASSN–15oi at late phases (∼330 d after discovery; Fig. 6). Upon further investigation, the L_{opt}/L_x ratio of both sources is nearly constant while the narrow lines are present (Fig. 10; see also Section 4.5). This suggests that the L_{opt}/L_x ratio evolution in ASASSN–15oi at late times may be similarly regulated by reprocessing of soft X-ray radiation in optically thick gas, analogous to the situation in AT 2018fyk and AGNs.

The formation of an accretion disc that radiates in soft X-rays, which subsequently partially ionize high density, optically thick gas surrounding the SMBH delivered by the disruption can explain the emergence of the Fe II emission lines. At the same time, the reprocessing of X-ray, Ly α, and/or EUV photons can power the plateau phase in the light curve, explaining both peculiar features in the TDE scenario. van Velzen et al. (2019b) showed that the late-time plateau phase can be explained by UV disc emission, and this can also contribute to the plateau phase seen in AT 2018fyk.

While high temporal coverage in X-ray and UV/optical wavelengths is available for only a few candidates, the UV/optical light-curve shape of AT 2018fyk is unique among UV/optical bright TDEs. If we are indeed witnessing the assembly of an accretion disc and reprocessing of disc X-ray radiation, this implies that it does not occur with a similar efficiency in most TDEs. The first 40 d of the light curve, however, show typical behaviour as observed in nearly all UV/optical TDEs (Fig. 8). The plateau represents an additional emission component superposed on the contribution responsible for the initial decline from peak. van Velzen et al. (2019b) showed that such a secondary maximum is observed in nearly all TDEs, but several years after disruption rather than several months as observed in AT 2018fyk and ASASSN–15lh.

4.4 Broad iron emission lines?

In terms of velocities, the He II 4686 and H α lines follow a similar trend, being consistent with their respective rest wavelengths in early epochs but becoming more blueshifted up to about 2000 km s^{-1}, with a blueshift of ∼1000 km s^{-1} in the latest spectrum. Although the He II 3202 line can tentatively be identified in the spectra, it is on the edge of the spectrum and a sudden decrease in instrumental throughput may instead be responsible for this feature. More interestingly, the (broad) line that we tentatively identify as O III at 3444 Å or He I at 3446 Å seems to be systematically redshifted by 2000–3000 km s^{-1}. Fitting a single Gaussian profile to this line, we find central wavelengths ranging between 3375 and 3500 Å during the evolution. However, the line has a rather boxy profile instead of being well described by a Gaussian. In this wavelength range, two narrow emission features with rest wavelength of 3449 and 3499 Å are visible during the nebular phase (Fig. 2). While the former is consistent with either O III 3444 Å or He I at 3447 Å, the identification of the latter is 3499 Å line is less secure. As an alternative, the NIST Atomic Spectra Data base shows several strong Fe II transitions corresponding to wavelengths close to 3449 and 3499 Å. If these line identifications as Fe II are correct, this provides unambiguous evidence for broad Fe II emission lines in the early spectroscopic observations (Fig. 2).

We also tentatively identify the emergence of a broad emission feature around He I 5876Å that is present in several epochs. Without a solid host galaxy subtraction, however, this feature must be interpreted with caution as it is unclear what constitutes the continuum level, given the many broad features and bumps present in the spectra. In addition, there is a deep absorption feature that distorts the line shape. We tentatively identify this feature as He I 5876Å but a proper host galaxy subtraction is needed to study the line evolution in more detail.

4.5 Optical to X-ray ratio evolution

AT 2018fyk is only the third TDE candidate with contemporaneous bright UV/optical and X-ray emission that has been observed by *Swift* with high cadence at both wavelength regimes. We show the ratio of integrated UV/optical luminosity to X-ray luminosity in Fig. 10, where we also overplot these ratios for ASASSN–14li, ASASSN–15oi, and AT2018zr (Gezari et al. 2017; van Velzen et al. 2019a). The L_{opt}/L_x ratio of ASASSN–14li is ∼1 for 400 d, with some hint of an increase at later times. On the other hand, the evolution of the L_{opt}/L_x ratio of ASASSN–15oi is markedly different, and has been interpreted as the delayed formation of an accretion disc (Gezari et al. 2017). The evolution of AT 2018fyk appears to broadly follow that of ASASSN–15oi, as it decreases over time. However, rather than a monotonic decrease sudden changes are apparent at early times and during the two most recent *Swift* observations. The L_{opt}/L_x ratio appears to plateau for ∼80 d similar to the UV/optical light curves, after which it decreases as the X-ray luminosity brightens and the X-ray spectrum becomes harder.

During this plateau phase, both the X-ray and UV/optical luminosity increase in tandem (compared to the initial decline) while narrow optical emission lines corresponding to He I and both permitted and forbidden transitions of O III appear in the spectrum. Given the high ionization potential (higher than 35 eV), these nebular lines O III lines typically only appear in the presence of

Table 4. Observed radio upper limits (stacked 16.7 and 21.2 GHz), compared to the radio luminosity expected for a radio–X-ray correlation similar to ASASSN–14li. The epoch denotes days after discovery.

Epoch (d)	$L_{\rm radio}$ (erg s^{-1})	$L_{\rm radio} \propto L_x^{2.2}$ (erg s^{-1})
11	$< 5 \times 10^{37}$	1×10^{36}
38	$< 1 \times 10^{38}$	1×10^{38}
75	$< 8 \times 10^{37}$	1×10^{38}

a strongly ionizing radiation field and relatively low densities. The absence of these lines in the early phases of the flare suggest that the ionizing source was much fainter at those times. A scenario where we are witnessing the formation of an accretion disc during the *Swift* observations can explain the nebular lines if the disc radiation ionizes debris (most likely the bound material, as the lines are observed at their rest wavelengths) from the disrupted star. The plateau in the light curve can then be explained as reprocessing of X-ray radiation into UV/optical photons, creating the right conditions for line emission. The disappearance of the nebular lines after the plateau indicate that the emitting layer of material has become fully ionized and optically thin to the X-ray radiation, which can explain the upturn in the XRT light curve while the UV/optical emission becomes fainter.

4.6 Radio upper limits

We can use the radio non-detections to constrain the presence of a jet/outflow similar to that observed in ASASSN–14li (Alexander et al. 2016; Romero-Cañizales et al. 2016; van Velzen et al. 2016a; Pasham & van Velzen 2018). To this end, we assume that the scaling relation between the radio and X-ray luminosity of a tentative jet/outflow is similar to that of ASASSN–14li, $L_r \propto L_x^{2.2}$ (Pasham & van Velzen 2018). From Table 4 we see that the observations can marginally rule out that such a jet was produced.

If the X-ray-radio jet coupling was similar to that seen in ASASSN–14li, the difference in jet power could be explained by either a difference in available accretion power for the jet to tap into (assuming a similar jet efficiency), or by a difference in the conversion efficiency from accretion power to jet power (Pasham & van Velzen 2018). While the latter is hard to test observationally, our observations disfavour the former scenario as the UV/optical and X-ray light curve and $L_{\rm opt}/L_{\rm x}$ evolution can potentially be explained by a relativistic encounter. Dai et al. (2015) have shown that this leads to higher accretion rates, hence this would result in a more powerful jet and more luminous radio emission if the jet power follows the mass accretion rate.

One scenario that could explain the radio non-detection is the presence of a tenuous circumnuclear medium (CNM; Generozov et al. 2017). Unfortunately, for AT 2018fyk, no strong constraints can be made. This illustrates the need for deeper radio observations to rule out the presence of a jet, even in the case of a low-density CNM. Upper limits several orders of magnitude deeper than those presented here are required to rule out a jet power similar to ASASSN–14li in known TDEs.

5 SUMMARY

We have presented and analysed multiwavelength photometric and spectroscopic observations of the UV/optical and X-ray bright tidal disruption event AT 2018fyk. *Gaia* observations of the transient constrain the transient position to within ∼120 pc of the galaxy nucleus. The densely sampled *Swift* UVOT and XRT light curves show a peculiar evolution when compared to other well-established TDEs but similar to ASASSN–15lh, including a secondary maximum after initial decline from peak. Optical spectra similarly showed peculiar features not previously identified, including both high- and low-ionization narrow emission features. We show that similar features were present in archival spectra of at least one other TDE (ASASSN–15oi), but remained unidentified due to the complex line profiles of the broad emission lines. The main results from our analysis can be summarized as follows:

(i) The X-ray and UV/optical light curves show a plateau phase of ∼50 d after an initial monotonic decline. When the UV/optical decline resumes, the X-rays instead turn over and increase in luminosity. Such a two-component light curve is similar to that seen in ASASSN–15lh, albeit on shorter time-scales. It can be naturally explained in the scenario of a TDE with relativistic pericentre, where the disc formation process is fast and efficient, resulting in this second maximum to occur 10–100s of days rather than 1000s of days after disruption, as observed for most TDEs (van Velzen et al. 2019b).

(ii) A high black hole mass ($\gtrsim 10^7$ $M_{\rm BH}$) can result in relativistic pericentres for a typical lower main-sequence star. We therefore suggest that, similar to ASASSN–15lh, the peculiar light curve of AT2018fyk is due to the high $M_{\rm BH}$, which can provide the right conditions to explain the light-curve shape. Moreover, we tentatively identify another double-peaked structure in the optical light curves of D3-13, which has $M_{\rm BH} \sim 10^{7.4}$ $M_\odot$. Double-peaked light curves might be a universal feature of TDEs around massive black holes ($M_{\rm BH} \gtrsim 10^7$ $M_\odot$) as the encounters are always expected to be relativistic.

(iii) The X-ray spectra can be relatively well described by an absorbed power law + blackbody model (power-law index ∼3, kT ∼ 110 eV). The power law contributes roughly 30 per cent of the flux even at early times. In the final two epochs of observations before the source became Sun constrained, the spectrum appears to develop a harder component above 2 keV. Continued monitoring and analysis will reveal whether a hard power-law tail appears, or whether the spectrum remains dominated by the soft (blackbody) component.

(iv) The optical spectra show broad H α and He II 4686 lines. We also tentatively identify broad Fe II lines at 3449Å and 3499 Å. In particular the He II 4686 line has a Gaussian FWHM significantly greater (∼28 × 10^3 km s^{-1}) than the other broad lines (∼10–15 × 10^3 km s^{-1}), suggesting it is a blend of multiple emission features.

(v) We detect both high-ionization (O III) and low-ionization (Fe II) narrow emission lines. In particular the Fe II complex near 4570 Å is unambiguously detected. We propose that this line complex can explain the asymmetric line profiles in this and several other Fe-rich TDEs (e.g. ASASSN–15oi, PTF–09ge).

(vi) The presence of low-ionization Fe II emission lines requires optically thick, high-density gas, and (most likely) a strong source of ionizing photons. Taken together with the light-curve evolution, this suggests that the X-ray radiation is (partially) being absorbed and efficiently re-emitted in the UV/optical. When the gas is sufficiently ionized it becomes optically thin to the X-rays, leading to a decline in the UV/optical emission and the observed increase in X-ray luminosity.

(vii) The spectral features are remarkably similar to those seen in NLS1 AGN, as well as very similar to other TDE candidates in AGN such as the extreme coronal line emitters. This suggests a connection between all these events around AGN and AT2018fyk, which occurred in a quiescent SMBH. This strengthens the arguments in favour of a TDE interpretation for PS16dtm, the Kankare et al. (2017) events and the coronal line emitters.

We have illustrated that a wealth of information can be extracted from contemporaneous X-ray and UV/optical observations made possible by *Swift* and spectroscopic monitoring, and shown the importance of dense temporal coverage to map the detailed behaviour of both the X-ray and UV/optical emission in TDEs. Increasing the sample of TDEs with such coverage will almost certainly lead to the discovery of new behaviour in these enigmatic cosmic lighthouses, which in turn will reveal the detailed physics that occurs in these extreme environments. The detection of narrow emission lines highlights the need for medium/high-resolution spectroscopic follow-up of TDEs to uncover the full diversity of their optical spectral appearance.

ACKNOWLEDGEMENTS

We are grateful for constructive remarks and suggestions from the referee. We also thank Richard Saxton for sharing the *Swift* data of XMMSL1 J0740, and Suvi Gezari for sharing some of the data in Fig. 10. TW is funded in part by European Research Council grant 320360 and by European Commission grant 730980. GL was supported by a research grant (19054) from VILLUM FONDEN. JCAM-J is the recipient of an Australian Research Council Future Fellowship (FT 140101082). PGJ and ZKR acknowledge support from European Research Council Consolidator Grant 647208. MG is supported by the Polish NCN MAESTRO grant 2014/14/A/ST9/00121. KM acknowledges support from STFC (ST/M005348/1) and from H2020 through an ERC Starting Grant (758638). MN acknowledges support from a Royal Astronomical Society Research Fellowship. FO acknowledges support of the H2020 Hemera program, grant agreement No 730970. Based on observations collected at the European Organisation for Astronomical Research in the Southern Hemisphere under ESO programme 199.D-0143. We acknowledge the use of public data from the Swift data archive. The Australia Telescope Compact Array is part of the Australia Telescope National Facility which is funded by the Australian Government for operation as a National Facility managed by CSIRO. This work has made use of data from the European Space Agency (ESA) mission *Gaia* (https://www.cosmos.esa.int/gaia), processed by the *Gaia* Data Processing and Analysis Consortium (DPAC, https://www.cosmos.esa.int/web/gaia/dpac/consortium). Funding for the DPAC has been provided by national institutions, in particular the institutions participating in the *Gaia* Multilateral Agreement. We also acknowledge the Gaia Photometric Science Alerts Team (http://gsaweb.ast.cam.ac.uk/alerts).

REFERENCES

Abramowicz M. A., Czerny B., Lasota J. P., Szuszkiewicz E., 1988, ApJ, 332, 646
Alexander K. D., Berger E., Guillochon J., Zauderer B. A., Williams P. K. G., 2016, ApJ, 819, L25
Arcavi I. et al., 2014, ApJ, 793, 38
Arnouts S., Cristiani S., Moscardini L., Matarrese S., Lucchin F., Fontana A., Giallongo E., 1999, MNRAS, 310, 540
Auchettl K., Guillochon J., Ramirez-Ruiz E., 2017, ApJ, 838, 149
Baldwin J. A., Ferland G. J., Korista K. T., Hamann F., LaCluyzé A., 2004, ApJ, 615, 610
Bersten M. C., Benvenuto O. G., Orellana M., Nomoto K., 2016, ApJ, 817, L8
Berton M. et al., 2015, A&A, 578, A28
Blagorodnova N. et al., 2017, ApJ, 844, 46
Blanchard P. K. et al., 2017, ApJ, 843, 106
Bloom J. S. et al., 2011, Science, 333, 203
Boller T., Freyberg M. J., Trümper J., Haberl F., Voges W., Nandra K., 2016, A&A, 588, A103
Bolton J. G., Gardner F. F., Mackey M. B., 1964, Aust. J. Phys., 17, 340
Bonnerot C., Lu W., 2019, preprint (arXiv:1906.05865)
Boroson T. A., Green R. F., 1992, ApJS, 80, 109
Brimacombe J. et al., 2018, Astron. Telegram, 12031
Bruzual G., Charlot S., 2003, MNRAS, 344, 1000
Burrows D. N. et al., 2005, Space Sci. Rev., 120, 165
Buzzoni B. et al., 1984, Messenger, 38, 9
Calzetti D., Armus L., Bohlin R. C., Kinney A. L., Koornneef J., Storchi-Bergmann T., 2000, ApJ, 533, 682
Cao R., Liu F. K., Zhou Z. Q., Komossa S., Ho L. C., 2018, MNRAS, 480, 2929
Cenko S. B. et al., 2012, ApJ, 753, 77
Chabrier G., 2003, PASP, 115, 763
Chen S. et al., 2018, A&A, 615, A167
Cutri R. M. et al., 2014, VizieR Online Data Catalog, p. II/328
Dai L., McKinney J. C., Miller M. C., 2015, ApJ, 812, L39
Dai L., McKinney J. C., Roth N., Ramirez-Ruiz E., Miller M. C., 2018, ApJ, 859, L20
Dong X.-B., Ho L. C., Wang J.-G., Wang T.-G., Wang H., Fan X., Zhou H., 2010, ApJ, 721, L143
Dong X.-B., Wang J.-G., Ho L. C., Wang T.-G., Fan X., Wang H., Zhou H., Yuan W., 2011, ApJ, 736, 86
Dong S. et al., 2016, Science, 351, 257
Dressler A., Gunn J. E., 1983, ApJ, 270, 7
Dwarkadas V. V., Gruszko J., 2012, MNRAS, 419, 1515
Fabricius C. et al., 2016, A&A, 595, A3
Foreman-Mackey D., Hogg D. W., Lang D., Goodman J., 2013, PASP, 125, 306
French K. D., Arcavi I., Zabludoff A., 2016, ApJ, 818, L21
Gaia Collaboration, 2016, A&A, 595, A1
Gaia Collaboration, 2018, A&A, 616, A1
Gallo L., 2018, Revisiting Narrow-line Seyfert 1 Galaxies and their Place in the Universe. Padova Botanical Garden, Italy, p. 34
Gehrels N. et al., 2004, ApJ, 611, 1005
Generozov A., Mimica P., Metzger B. D., Stone N. C., Giannios D., Aloy M. A., 2017, MNRAS, 464, 2481
Gezari S. et al., 2008, ApJ, 676, 944
Gezari S., Cenko S. B., Arcavi I., 2017, ApJ, 851, L47
Godoy-Rivera D. et al., 2017, MNRAS, 466, 1428
Graham M. J., Clowes R. G., Campusano L. E., 1996, MNRAS, 279, 1349
Greiner J., Schwarz R., Zharikov S., Orio M., 2000, A&A, 362, L25
Guillochon J., Ramirez-Ruiz E., 2015, ApJ, 809, 166
Guillochon J., Manukian H., Ramirez-Ruiz E., 2014, ApJ, 783, 23
Häring N., Rix H.-W., 2004, ApJ, 604, L89
Hills J. G., 1975, Nature, 254, 295
Hodgkin S. T., Wyrzykowski L., Blagorodnova N., Koposov S., 2013, Phil. Trans. R. Soc. A, 371, 20120239
Holoien T. W. S. et al., 2016a, MNRAS, 455, 2918
Holoien T. W. S. et al., 2016b, MNRAS, 463, 3813
Holoien T. W. S. et al., 2019, ApJ, 880, 120
Horne K., 1986, PASP, 98, 609
Hung T. et al., 2017, ApJ, 842, 29
Hung T. et al., 2019, ApJ, 879, 119
Ilbert O. et al., 2006, A&A, 457, 841
Jansen F. et al., 2001, A&A, 365, L1
Jiang N., Dou L., Wang T., Yang C., Lyu J., Zhou H., 2016, ApJ, 828, L14
Kankare E. et al., 2017, Nat. Astron., 1, 865
Kennicutt R. C., Jr., 1998, ARA&A, 36, 189

Kochanek C. S. et al., 2017, PASP, 129, 104502
Komossa S., Bade N., 1999, A&A, 343, 775
Kostrzewa-Rutkowska Z. et al., 2018, MNRAS, 481, 307
Kovačević J., Popović L. Č., Dimitrijević M. S., 2010, ApJS, 189, 15
Kwan J., Krolik J. H., 1981, ApJ, 250, 478
Lawrence A., Saunders W., Rowan-Robinson M., Crawford J., Ellis R. S., Frenk C. S., Efstathiou G., Kaiser N., 1988, MNRAS, 235, 261
Law N. M. et al., 2009, PASP, 121, 1395
Leloudas G. et al., 2016, Nat. Astron., 1, 0002
Leloudas G. et al., 2019, (arXiv: e-prints)
Lindegren L. et al., 2018, A&A, 616, A2
Liu F. K., Zhou Z. Q., Cao R., Ho L. C., Komossa S., 2017, MNRAS, 472, L99
Loeb A., Ulmer A., 1997, ApJ, 489, 573
Margutti R. et al., 2017, ApJ, 836, 25
Margutti R. et al., 2018, ApJ, 864, 45
Marinello M., Rodríguez-Ardila A., Garcia-Rissmann A., Sigut T. A. A., Pradhan A. K., 2016, ApJ, 820, 116
Mattila S. et al., 2018, Science, 361, 482
McMullin J. P., Waters B., Schiebel D., Young W., Golap K., 2007, in Shaw R. A., Hill F., Bell D. J., eds, ASP Conf. Ser. Vol. 376, Astronomical Data Analysis Software and Systems XVI. Astron. Soc. Pac., San Francisco, p. 127
Metzger B. D., Stone N. C., 2016, MNRAS, 461, 948
Netzer H., Wills B. J., 1983, ApJ, 275, 445
Osterbrock D. E., Pogge R. W., 1985, ApJ, 297, 166
Pasham D. R., van Velzen S., 2018, ApJ, 856, 1
Peterson B. M., 2011, in Narrow-Line Seyfert 1 Galaxies and their Place in the Universe, Proceedings of Science, PoS(NLS1), p. 32
Phinney E. S., 1989, in Morris M., ed., Proc. IAU Symp. 136, The Center of the Galaxy. Kluwer, Dordrecht, p. 543
Piran T., Svirski G., Krolik J., Cheng R. M., Shiokawa H., 2015, ApJ, 806, 164
Planck Collaboration XVI, 2014, A&A, 571, A16
Rakshit S., Stalin C. S., Chand H., Zhang X.-G., 2017, ApJS, 229, 39
Rees M. J., 1988, Nature, 333, 523
Roelofs G. H. A., Groot P. J., Marsh T. R., Steeghs D., Nelemans G., 2006, MNRAS, 365, 1109
Romero-Cañizales C., Prieto J. L., Chen X., Kochanek C. S., Dong S., Holoien T. W.-S., Stanek K. Z., Liu F., 2016, ApJ, 832, L10
Roming P. W. A. et al., 2005, Space Sci. Rev., 120, 95
Roth N., Kasen D., 2018, ApJ, 855, 54
Roth N., Kasen D., Guillochon J., Ramirez-Ruiz E., 2016, ApJ, 827, 3
Savage A., Bolton J. G., Wright A. E., 1977, MNRAS, 179, 135
Saxton R. D., Read A. M., Komossa S., Lira P., Alexander K. D., Wieringa M. H., 2017, A&A, 598, A29
Shappee B. J. et al., 2014, ApJ, 788, 48
Shiokawa H., Krolik J. H., Cheng R. M., Piran T., Noble S. C., 2015, ApJ, 804, 85
Sigut T. A. A., Pradhan A. K., 1998, ApJ, 499, L139
Smartt S. J. et al., 2015, A&A, 579, A40
Stern D. et al., 2012, ApJ, 753, 30
Stone N., Sari R., Loeb A., 2013, MNRAS, 435, 1809
Stone N. C., Generozov A., Vasiliev E., Metzger B. D., 2018, MNRAS, 480, 5060
Stoughton C. et al., 2002, AJ, 123, 485
Strubbe L. E., Quataert E., 2009, MNRAS, 400, 2070
Ulmer A., 1999, ApJ, 514, 180
van Velzen S. et al., 2011, ApJ, 741, 73
van Velzen S. et al., 2016a, Science, 351, 62
van Velzen S., Mendez A. J., Krolik J. H., Gorjian V., 2016b, ApJ, 829, 19
van Velzen S. et al., 2019a, ApJ, 872, 198
van Velzen S., Stone N. C., Metzger B. D., Gezari S., Brown T. M., Fruchter A. S., 2019b, ApJ, 878, 82
Veron-Cetty M. P., Veron P., 1983, A&AS, 53, 219
Wang T.-G., Zhou H.-Y., Wang L.-F., Lu H.-L., Xu D., 2011, ApJ, 740, 85
Wevers T., van Velzen S., Jonker P. G., Stone N. C., Hung T., Onori F., Gezari S., Blagorodnova N., 2017, MNRAS, 471, 1694
Wevers T. et al., 2018, Astron. Telegram, 12040
Wevers T. et al., 2019, MNRAS, 487, 4136
Wu X.-B., Hao G., Jia Z., Zhang Y., Peng N., 2012, AJ, 144, 49
Wyrzykowski Ł. et al., 2017, MNRAS, 465, L114
Yang C.-W., Wang T.-G., Ferland G., Yuan W., Zhou H.-Y., Jiang P., 2013, ApJ, 774, 46
Zhang X.-G., Dultzin-Hacyan D., Wang T.-G., 2006, MNRAS, 372, L5

SUPPORTING INFORMATION

Supplementary data are available at *MNRAS* online.

AT2018fyk_swift_mrtable.txt

Please note: Oxford University Press is not responsible for the content or functionality of any supporting materials supplied by the authors. Any queries (other than missing material) should be directed to the corresponding author for the article.

APPENDIX A: *SWIFT* UVOT OBSERVATIONS

Table A1. *Swift* UVOT host unsubtracted photometry, in Vega magnitudes, and the *Swift* XRT count rates for each observation ID. The conversion factor from count rate to flux used in this work is 4.41×10^{-11}. We provide the mean MJD of the reference times in the UVOT bands. This table will be made available in machine-readable form.

MJD (d)	*U* (mag)	*B* (mag)	*V* (mag)	*UVW1* (mag)	*UVM2* (mag)	*UVW2* (mag)	XRT (counts s^{-1})
58383.7279	15.9 ± 0.06	16.96 ± 0.07	16.39 ± 0.09	15.1 ± 0.04	14.92 ± 0.03	14.61 ± 0.03	0.005 ± 0.0018
58389.9486	16.0 ± 0.07	16.92 ± 0.08	16.72 ± 0.14	15.13 ± 0.05	14.94 ± 0.04	14.76 ± 0.04	0.055 ± 0.0092
58393.1195	16.01 ± 0.09	17.01 ± 0.11	16.42 ± 0.15	15.33 ± 0.06	14.98 ± 0.05	14.8 ± 0.04	0.033 ± 0.0092
58395.7247	16.05 ± 0.07	17.19 ± 0.09	16.54 ± 0.12	15.4 ± 0.05	15.05 ± 0.04	14.9 ± 0.04	0.025 ± 0.0031
58396.2499	16.07 ± 0.09	17.17 ± 0.11	16.54 ± 0.15	15.39 ± 0.06	15.07 ± 0.05	14.9 ± 0.04	0.020 ± 0.0075
58397.9151	16.18 ± 0.06	17.09 ± 0.07	16.59 ± 0.1	15.44 ± 0.04	15.22 ± 0.04	15.05 ± 0.03	0.048 ± 0.0054
58398.979	16.28 ± 0.09	17.15 ± 0.1	16.66 ± 0.14	15.51 ± 0.06	15.22 ± 0.05	15.05 ± 0.04	0.046 ± 0.0091
58399.7422	16.29 ± 0.09	17.4 ± 0.11	16.73 ± 0.14	15.58 ± 0.06	15.29 ± 0.04	15.13 ± 0.04	0.032 ± 0.0039
58401.1307	16.2 ± 0.08	17.25 ± 0.1	16.55 ± 0.15	15.58 ± 0.06	15.35 ± 0.05	15.12 ± 0.04	0.030 ± 0.0049
58403.7488	16.39 ± 0.11	17.27 ± 0.12	16.7 ± 0.16	15.63 ± 0.07	15.35 ± 0.05	15.2 ± 0.05	0.038 ± 0.0100
58404.5755	16.49 ± 0.08	17.42 ± 0.09	16.63 ± 0.11	15.63 ± 0.05	15.31 ± 0.07	15.28 ± 0.04	0.051 ± 0.0064
58406.1341	16.54 ± 0.1	17.23 ± 0.1	16.74 ± 0.15	15.71 ± 0.06	15.45 ± 0.05	15.42 ± 0.05	0.035 ± 0.0077
58408.4551	16.27 ± 0.1	16.99 ± 0.11	16.64 ± 0.16	15.61 ± 0.07	15.39 ± 0.05	15.23 ± 0.05	0.035 ± 0.0084

Table A1 *– continued*

MJD (d)	*U* (mag)	*B* (mag)	*V* (mag)	*UVW*1 (mag)	*UVM*2 (mag)	*UVW*2 (mag)	XRT (counts s^{-1})
58409.9907	16.39 ± 0.07	17.29 ± 0.07	16.5 ± 0.09	15.74 ± 0.05	15.46 ± 0.04	15.25 ± 0.04	0.026 ± 0.0047
58412.3747	16.1 ± 0.1	17.4 ± 0.14	16.68 ± 0.17	15.75 ± 0.07	15.46 ± 0.05	15.35 ± 0.05	0.041 ± 0.0100
58413.9073	16.31 ± 0.06	17.32 ± 0.07	16.73 ± 0.09	15.63 ± 0.04	15.39 ± 0.03	15.21 ± 0.03	0.034 ± 0.0048
58415.9641	16.25 ± 0.09	17.08 ± 0.09	16.55 ± 0.13	15.71 ± 0.06	15.38 ± 0.05	15.24 ± 0.04	0.041 ± 0.0086
58416.1691	16.3 ± 0.1	17.13 ± 0.11	16.45 ± 0.14	15.66 ± 0.07	15.44 ± 0.05	15.18 ± 0.05	0.028 ± 0.0083
58417.3639	16.38 ± 0.11	17.03 ± 0.11	16.79 ± 0.18	15.59 ± 0.07	15.48 ± 0.06	15.31 ± 0.05	0.024 ± 0.0079
58417.8613	16.25 ± 0.07	17.24 ± 0.08	16.7 ± 0.11	15.73 ± 0.05	15.4 ± 0.04	15.2 ± 0.04	0.062 ± 0.0061
58418.6338	16.23 ± 0.1	17.21 ± 0.12	16.65 ± 0.16	15.65 ± 0.07	15.44 ± 0.05	15.24 ± 0.05	0.043 ± 0.0098
58420.1548	16.3 ± 0.1	17.24 ± 0.11	16.83 ± 0.17	15.58 ± 0.07	15.43 ± 0.05	15.15 ± 0.05	0.058 ± 0.012
58421.8815	16.29 ± 0.07	17.44 ± 0.09	16.47 ± 0.1	15.61 ± 0.05	15.45 ± 0.04	15.22 ± 0.04	0.033 ± 0.0057
58423.5402	16.31 ± 0.09	17.13 ± 0.1	16.42 ± 0.12	15.7 ± 0.06	15.38 ± 0.05	15.16 ± 0.04	0.035 ± 0.0083
58425.0384	16.24 ± 0.06	17.18 ± 0.07	16.59 ± 0.1	15.58 ± 0.04	15.34 ± 0.04	15.2 ± 0.03	0.066 ± 0.0063
58426.5273	16.22 ± 0.09	17.23 ± 0.11	16.68 ± 0.16	15.54 ± 0.07	15.36 ± 0.06	15.19 ± 0.05	0.053 ± 0.012
58427.323	16.3 ± 0.1	17.08 ± 0.1	16.49 ± 0.14	15.57 ± 0.06	15.34 ± 0.05	15.17 ± 0.05	0.035 ± 0.0091
58428.8499	16.28 ± 0.09	17.29 ± 0.11	16.52 ± 0.13	15.69 ± 0.06	15.3 ± 0.04	15.12 ± 0.04	0.088 ± 0.012
58429.8529	16.21 ± 0.08	17.22 ± 0.09	16.47 ± 0.11	15.47 ± 0.05	15.32 ± 0.04	15.13 ± 0.04	0.033 ± 0.0075
58430.0486	16.25 ± 0.08	16.94 ± 0.09	16.51 ± 0.13	15.53 ± 0.06	15.35 ± 0.05	15.12 ± 0.04	0.061 ± 0.011
58431.5081	16.21 ± 0.09	17.14 ± 0.1	16.64 ± 0.15	15.58 ± 0.06	15.35 ± 0.05	15.1 ± 0.04	0.071 ± 0.011
58434.9552	16.19 ± 0.08	17.07 ± 0.09	16.61 ± 0.12	15.59 ± 0.06	15.28 ± 0.06	15.19 ± 0.04	0.069 ± 0.012
58439.075	16.16 ± 0.09	16.93 ± 0.09	16.72 ± 0.15	15.61 ± 0.07	15.35 ± 0.07	15.13 ± 0.05	0.063 ± 0.013
58440.0052	16.31 ± 0.08	17.24 ± 0.09	16.72 ± 0.12	15.44 ± 0.06	15.35 ± 0.05	15.16 ± 0.04	0.033 ± 0.0060
58443.2648	16.33 ± 0.08	17.18 ± 0.08	16.62 ± 0.12	15.63 ± 0.06	15.35 ± 0.06	15.19 ± 0.04	0.039 ± 0.0091
58445.3327	16.28 ± 0.07	17.2 ± 0.08	16.74 ± 0.12	15.63 ± 0.06	15.43 ± 0.06	15.31 ± 0.04	0.024 ± 0.0073
58447.9741	16.46 ± 0.09	17.2 ± 0.1	16.65 ± 0.13	15.74 ± 0.07	15.41 ± 0.08	15.26 ± 0.04	0.049 ± 0.011
58449.0333	16.4 ± 0.1	17.28 ± 0.12	16.36 ± 0.13	15.89 ± 0.09	15.53 ± 0.07	15.36 ± 0.05	0.031 ± 0.0090
58451.3648	16.58 ± 0.09	17.32 ± 0.09	16.7 ± 0.12	15.93 ± 0.07	15.67 ± 0.06	15.5 ± 0.05	0.029 ± 0.0074
58455.5525	16.4 ± 0.08	17.29 ± 0.09	16.73 ± 0.13	15.94 ± 0.07	15.68 ± 0.07	15.61 ± 0.05	0.0069 ± 0.0040
58459.9956	16.8 ± 0.11	17.4 ± 0.11	16.6 ± 0.12	16.24 ± 0.09	15.88 ± 0.07	15.64 ± 0.05	0.016 ± 0.0057
58464.6536	16.63 ± 0.07	17.47 ± 0.08	16.68 ± 0.1	16.07 ± 0.06	15.9 ± 0.06	15.76 ± 0.04	0.021 ± 0.0051
58467.7725	16.69 ± 0.07	17.51 ± 0.08	16.68 ± 0.09	16.2 ± 0.06	15.96 ± 0.06	15.78 ± 0.04	0.020 ± 0.0045
58470.4318	16.81 ± 0.08	17.52 ± 0.08	16.79 ± 0.1	16.31 ± 0.07	16.07 ± 0.06	15.84 ± 0.04	0.022 ± 0.0050
58473.8851	16.86 ± 0.08	17.47 ± 0.08	16.7 ± 0.09	16.13 ± 0.06	15.92 ± 0.06	15.82 ± 0.04	0.029 ± 0.0055
58476.373	17.17 ± 0.11	17.4 ± 0.09	16.73 ± 0.11	16.39 ± 0.08	16.0 ± 0.06	15.93 ± 0.05	0.041 ± 0.0045
58479.9228	16.75 ± 0.09	17.5 ± 0.11	16.63 ± 0.11	16.36 ± 0.08	16.12 ± 0.07	15.8 ± 0.05	0.039 ± 0.0076
58482.0515	16.98 ± 0.09	17.49 ± 0.09	16.83 ± 0.11	16.56 ± 0.08	16.37 ± 0.07	16.22 ± 0.05	0.024 ± 0.0055
58485.2343	17.13 ± 0.11	17.75 ± 0.12	16.93 ± 0.12	16.73 ± 0.09	16.49 ± 0.08	16.25 ± 0.05	0.063 ± 0.0089
58491.9408	17.09 ± 0.11	17.76 ± 0.12	16.85 ± 0.12	16.81 ± 0.1	16.53 ± 0.08	16.32 ± 0.06	0.080 ± 0.010

[1]*Institute of Astronomy, University of Cambridge, Madingley Road, Cambridge CB3 0HA, UK*
[2]*MIT Kavli Institute for Astrophysics and Space Research, Cambridge, MA 02139, USA*
[3]*Department of Astronomy, University of Maryland, College Park, MD 20742, USA*
[4]*Center for Cosmology and Particle Physics, New York University, New York, NY 10003, USA*
[5]*DTU Space, National Space Institute, Technical University of Denmark, Elektrovej 327, DK-2800 Kgs. Lyngby, Denmark*
[6]*Department of Particle Physics and Astrophysics, Weizmann Institute of Science, Rehovot 7610001, Israel*
[7]*ICRAR - Curtin University, GPO Box U1987, Perth, WA 6845, Australia*
[8]*SRON, Netherlands Institute for Space Research, Sorbonnelaan 2, NL-3584 CA Utrecht, the Netherlands*
[9]*Department of Astrophysics/IMAPP, Radboud University, P.O. Box 9010, NL-6500 GL Nijmegen, the Netherlands*
[10]*Warsaw University Astronomical Observatory, Al. Ujazdowskie 4, PL-00-478 Warszawa, Poland*
[11]*Tuorla Observatory, Department of Physics and Astronomy, University of Turku, Väisäläntie 20, FI-21500 Piikkiö, Finland*
[12]*Nordic Optical Telescope, Apartado 474, E-38700 Santa Cruz de La Palma, Spain*
[13]*Finnish Centre for Astronomy with ESO (FINCA), University of Turku, Quantum, Vesilinnantie 5, FI-20014 University of Turku, Finland*
[14]*Aalto University Metsähovi Radio Observatory, Metsähovintie 114, FI-02540 Kylmälä, Finland*
[15]*Astrophysics Research Centre, School of Mathematics and Physics, Queens University Belfast, Belfast BT7 1NN, UK*
[16]*School of Physics, Trinity College Dublin, Dublin D02 PN40 , UK*
[17]*Istituto di Astrofisica e Planetologia Spaziali (INAF), via del Fosso del Cavaliere 100, Roma I-00133, Italy*
[18]*Institute for Astronomy, University of Edinburgh, Royal Observatory, Blackford Hill, Edinburgh EH9 3HJ, UK*
[19]*Birmingham Institute for Gravitational Wave Astronomy and School of Physics and Astronomy, University of Birmingham, Birmingham B15 2TT, UK*

This paper has been typeset from a TEX/LATEX file prepared by the author.